Available online at www.sciencedirect.com
ScienceDirect
Trans. Nonferrous Met. Soc. China 35(2025) 888−901
Transactions of Nonferrous Metals Society of China
www.tnmsc.cn

Effect of trace cerium addition on hot deformation behavior of ultrahigh-purity copper containing sulfur

Ke-xing SONG[1,2], Yun-xiao HUA[1], Hai-tao LIU[1,3],
Yan-min ZHANG[1,3], Chao-min ZHANG[1,3], Yan-jun ZHOU[1,3], Tao HUANG[1,3]

1. School of Materials Science and Engineering, Henan University of Science and Technology, Luoyang 471023, China;
2. Institute of Materials, Henan Academy of Sciences, Zhengzhou 450046, China;
3. Provincial and Ministerial Co-construction of Collaborative Innovation Center of Nonferrous New Materials and Advanced Processing Technology, Luoyang 471023, China

Received 31 July 2023; accepted 9 April 2024

Abstract: The effects of trace cerium (Ce) addition on the microstructural and textural evolution and the dynamic recrystallization (DRX) of the ultrahigh-purity copper (Cu) containing small amounts of sulfur (S) were investigated using a Gleeble−1500 thermal simulation tester at 600 °C. The results show that with increasing Ce content, the grain size of the Cu−S (S2) alloy gradually decreases and the grain boundary embrittlement induced by S impurities is considerably inhibited. The addition of Ce promotes the DRX process of the S2 alloy and changes its DRX mechanism from discontinuous to continuous and twinning-induced DRX mechanisms. The texture component and intensity of the S2 alloy vary with the increase of Ce content. The addition of 120×10^{-6} Ce (mass fraction) is favorable for the grain orientation randomization, which is attributed to the promoted DRX.

Key words: Ce addition; S impurities; ultrahigh-purity copper; microstructure; dynamic recrystallization; texture

1 Introduction

Copper (Cu) and its alloys have excellent mechanical properties, thermal conductivity, and corrosion resistance. Thus, they are widely used in the aerospace and transportation industries and electronic communication, becoming indispensable materials for social development. Generally, Cu materials contain impurity elements, particularly S, since Cu ores primarily exist as sulfides in nature. Moreover, the sulfuric acid–copper sulfate system is used for electrolytic refining of pure Cu. S impurities in Cu usually cause grain boundary embrittlement (GBE) and considerably decrease the ductility during hot working [1−4]. The ultrahigh-purity Cu containing 53×10^{-6} S (mass fraction) undergoes GBE at 300−750 °C due to the formation of brittle Cu−S phases and their phase transformation at the grain boundaries (GBs) [4]. However, the effect of trace S impurities on the deformation behavior of ultrahigh-purity Cu and the modification of GBE induced by S impurities during hot working have been rarely reported.

Microalloying is an effective way to modify the microstructure of metallic materials and thus improve their mechanical properties. As the vitamins of modern industry, rare-earth elements (REs) are extensively used as alloying additives to steels [5−7], aluminum alloys [8−10] and magnesium alloys [11−13], which can remove the impurities and significantly improve the processing

Corresponding author: Yun-xiao HUA, Tel: +86-15236213121, E-mail: huayunxiao@163.com;
Hai-tao LIU, Tel: +86-15538838918, E-mail: htliu1204@haust.edu.cn
DOI: https://doi.org/10.1016/S1003-6326(24)66721-X

performance of materials. Similarly, REs in Cu alloys, such as Y, Ce, and La, have also shown beneficial effects on microstructural modification, thereby enhancing the processing properties [14−18]. XU et al [19] found that the addition of Y element can promote the DRX and weaken the texture of the Cu−Sn−Ni−Zn−Ti alloy, which improved the thermal deformation ability. The effects of Ce on the hot deformation behavior of the Cu−Zr−Cr [20], Cu−Mg [21] and Cu−Mg−Fe alloys [22] were studied. Their results showed that the addition of Ce produced grain refinement and increased the flow stress, optimizing the hot workability of alloys. It can be seen that the addition of REs can effectively improve the hot-working properties of Cu materials via grain refinement and texture weakening. However, the role of REs in the hot deformation of Cu or Cu-based alloys containing trace S impurities is unclear. Therefore, the effect of REs on the deformation behavior of Cu−S alloys must be comprehensively studied for developing the high-performance Cu-based materials.

In this work, in order to eliminate the effect of other impurities, Cu with an ultrahigh-purity of 99.99999% (7N) is selected as the raw material. The S2 alloy containing 53×10^{-6} S from our previous study [4] is chosen as the research object. The effects of trace Ce addition on the deformation behavior of the S2 alloy, including the microstructural and textural evolution as well as the DRX during hot compression are systematically investigated. Our findings comprehensively reveal the effect of S impurities with trace concentration on the hot deformation behavior of 7N Cu, which provides an effective way for the inhibition of GBE induced by trace S impurities and thus the significant improvement of the hot working performance for Cu and Cu-based alloys.

2 Experimental

Three Cu ingots, named S2, SC1 and SC2, were produced by vacuum induction melting under a pure Ar atmosphere at 6×10^4 Pa. The electrolytic Cu with an ultrahigh-purity of 99.99999% purchased from the Henan Guoxi Ultrapure New Materials Co., Ltd. was used as the raw material for melting. The S and Ce elements with purities of 99.99% were enwrapped by pure Cu foils and added into the Cu melt via secondary feeding. After the ingots were cooled to room temperature, the casting risers were cut off and the surfaces were turned. Then the ingots were annealed at 900 °C for 1 h and then extruded in one step with a final outer diameter of 20 mm. The chemical compositions were determined by inductively-coupled-plasma atomic emission spectrometry method (GB/T 5121.27—2008), as shown in Table 1. The results of three independent specimens were averaged, and the errors of the three investigated alloys were within the range of $(3-6)\times10^{-6}$.

Cylindrical specimens with a diameter of 8 mm and height of 12 mm were machined with the compression axis parallel to the extrusion direction (ED) from the as-extruded rods. All the samples were annealed at (450 °C, 1 h)+(650 °C, 1 h)+(950 °C, 0.5 h) in a tube furnace with flowing Ar gas, and then immediately quenched in ice water. Compression tests were conducted using a Gleeble−1500 thermal–mechanical simulation tester at a strain rate of 1.0×10^{-2} s^{-1} and stopped under different strains at 600 °C. Water quenching was applied to preserving the high-temperature structures. The deformed samples were cut along the compression axis diameter by electrical discharge machining, and then ground and polished through ion milling in Leica EM RES102 instrument. Electron backscatter diffraction (EBSD) was performed on OXFORD NordlysMax2 to investigate the microstructural and textural evolution and DRX during hot compression. A lower-limit boundary-misorientation cutoff of 2° was used, and a criterion of 15° was used to differentiate low-angle GBs (LAGBs) and high-angle GBs (HAGBs). The major texture components

Table 1 Impurity content from S2, SC1 and SC2 samples obtained by analytical chemistry (10^{-6})

Sample	Zn	Si	Ag	Pb	Fe	Bi	P	S	Ce
S2	0.013	0.006	0.08	0.007	0.003	0.005	0.007	53	−
SC1	0.017	0.009	0.13	0.006	0.008	0.003	0.004	58	78
SC2	0.012	0.009	0.08	0.007	0.007	0.004	0.005	55	120

were counted with a deviation angle of ±10°. The nucleation of recrystallized grains was studied via transmission electron microscopy (TEM), for which specimens were prepared from pre-characterized profiles. TEM investigations were carried out on a FEI Talos F200X microscope equipped with a high-brightness field emission gun and a monochromator operating at 200 keV.

3 Results and discussion

3.1 Initial microstructure and texture

Figure 1 shows the EBSD analysis of the three samples before hot compression, including their orientation maps and corresponding misorientation distributions as well as the inverse pole figures (IPFs). It is clear that the addition of Ce has an evident refining effect on the microstructure of S2 alloy, showing that the average grain sizes of the S2, SC1 and SC2 alloys are 132.7, 103.6 and 102.4 μm, respectively, as presented in Figs. 1(a–c). This is mainly attributed to the dragging effect of the dissolved Ce atoms and the pinning effect of Ce−S precipitates on GBs during the high-temperature solid-solution process. After annealing, these alloys mainly contain HAGBs, the volume fractions of which are 91.7%, 97.9% and 91.6%, respectively, as shown in Figs. 1(d−f). Figures 1(g−i) provide the IPFs of the alloys, wherein the grains with ⟨111⟩ orientation are dominant in the S2 alloy, which has a high texture intensity of 8.31. After trace Ce is added, the grain orientation of the S2 alloy becomes more randomized and the texture intensity significantly decreases to 2.73 and 3.2, respectively. Similar to the S2 alloy, the grains with ⟨111⟩ orientation are dominant in the SC1 alloy, but the volume fraction of the ⟨100⟩-oriented grains evidently increases. However, in the SC2 alloy with a higher Ce content, most grains have an orientation of ⟨110⟩, causing a slight increase in texture intensity compared to that of the SC1 alloy.

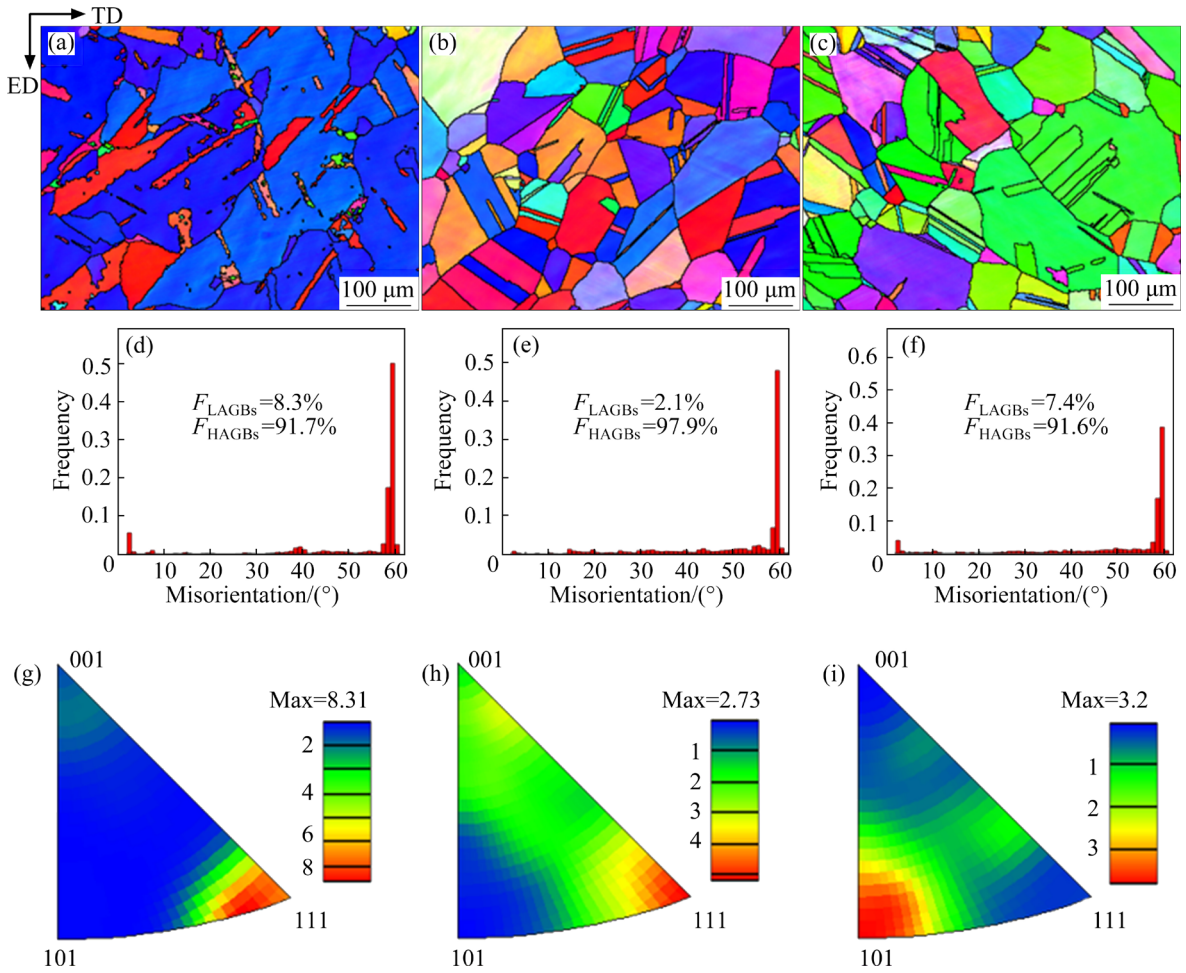

Fig. 1 Orientation maps (a–c), misorientation distribution maps (d–f), and inverse pole figures (g–i) of S2 (a, d, g), SC1 (b, e, h), and SC2 (c, f, i) alloys before hot compression

3.2 True stress–strain curves

Figure 2 shows the true stress–strain curves and the corresponding peak stresses of the S2, SC1 and SC2 alloys during the hot compression at 600 °C. The true stress–strain curves of these alloys exhibit similar variation trends as the strain increases. The flow stress first reaches a peak value and then slowly decreases, with the corresponding strain of ~0.3 for the peak stress. In general, the thermal deformation of materials is relevant to work-hardening, dynamic recovery (DRV) and DRX. In the early stage of deformation, dislocations rapidly multiplicate and tangle, leading to a significant increase in deformation resistance and thus an obvious improvement in flow stress. Then, driven by the deformation storage energy, the samples undergo the DRV or DRX, resulting in a decrease in flow stress [23,24]. In Fig. 2(a), it is observed that the flow stresses of the three alloys gradually decrease after reaching their peak values. This indicates the occurrence of DRX, which softens the alloys and enhances their plastic deformation ability. Figure 2(b) shows that the peak stresses of the S2, SC1 and SC2 alloys are 77.9, 77.4 and 83.6 MPa, respectively, suggesting that Ce can strengthen the S2 alloy only when its addition exceeds a certain content.

3.3 Microstructural evolution

Figure 3 illustrates the microstructural evolution of the S2, SC1 and SC2 alloys during hot compression at 600 °C, the corresponding average grain sizes are presented in Fig. 4. At the initial deformation stage, the average grain size of the S2 alloy decreases from 146.5 to 135.4 μm with the increase of Ce content. This suggests that the addition of trace amounts of Ce does not contribute to an obvious grain refinement of S2 alloy under a small deformation amount. Moreover, it is noted that the grain coarsening occurs in all the alloys compared to that before the compression, indicating that the grain boundary migration results in grain growth due to the high-temperature deformation. In addition, small amounts of DRX grains are observed in the SC2 alloy, as presented in Fig. 3(g). Most of these grains nucleate and grow along the twin boundaries (TBs), indicating that adding a certain amount of Ce is favorable for twinning-induced DRX in Cu−S alloy.

With the increase of deformation to 40%, the average grain sizes of the S2, SC1 and SC2 alloys decrease owing to the proliferation and tangling of high-density dislocations that cause grain elongation and fragmentation and DRX causes grain refinement. It is observed that the S2 alloy undergoes a severe intergranular cracking, which is due to the formation of brittle Cu−S phases and their phase transformation behavior at GBs, as reported in our previous work [4]. Figures 3(e, h) show that the intergranular embrittlement of the S2 alloy is significantly inhibited after addition of trace Ce. However, the SC1 alloy still retains some of the characteristics of intergranular cracking because of the lower Ce content, while no cracks at GBs are observed in the SC2 alloy containing a higher Ce content. Moreover, the content of sub-grain boundaries in the SC1 and SC2 alloys increases compared to the initial deformation stage. In the SC1 alloy, the sub-grains inside the grains rotate to form new DRX grains, and the TBs act as the nucleation sites for the small DRX grains, similar to the SC2 alloy shown in Fig. 3(g).

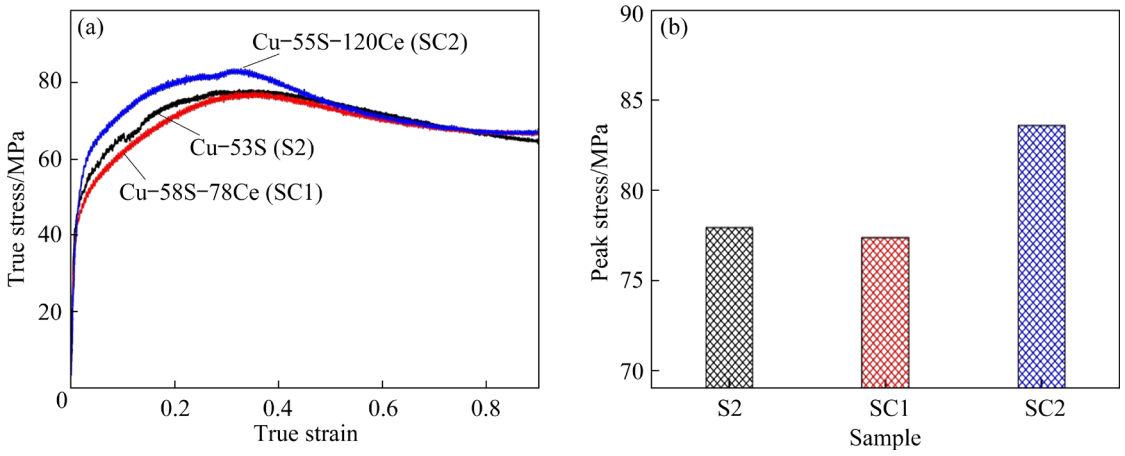

Fig. 2 True stress–strain curves (a) and peak stresses (b) of S2, SC1 and SC2 alloys during hot compression at 600 °C

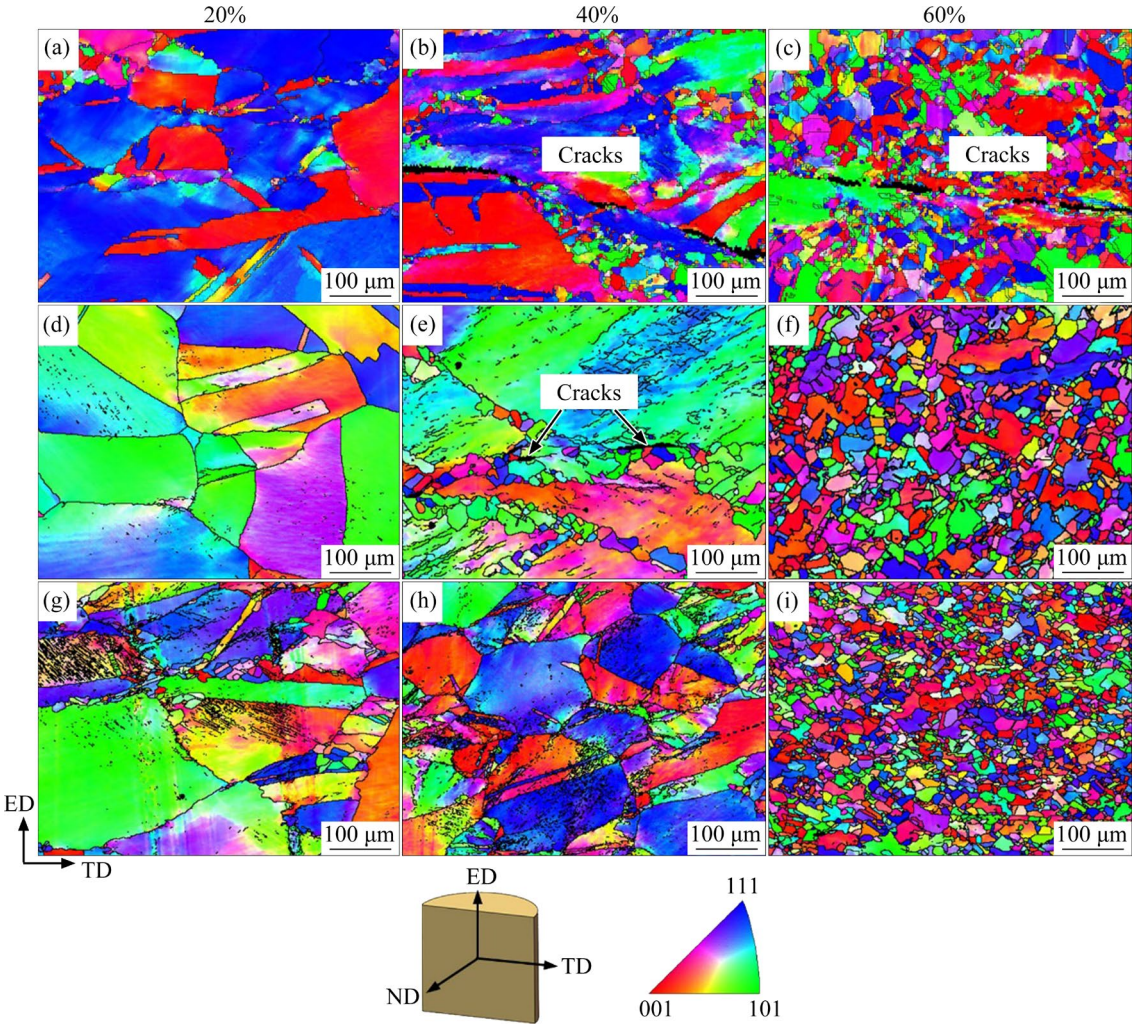

Fig. 3 Microstructural evolution of S2 (a–c), SC1 (d–f), and SC2 (g–i) alloys during hot compression at 600 °C and different deformations

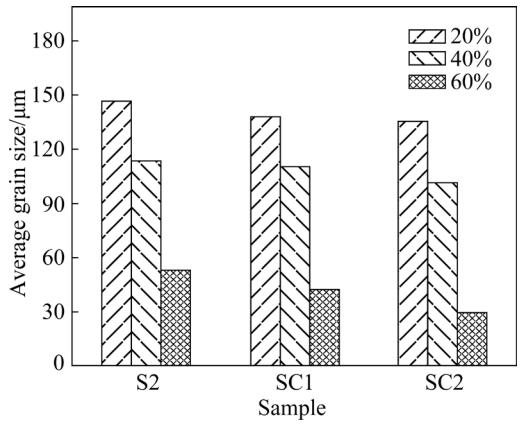

Fig. 4 Average grain sizes of S2, SC1 and SC2 alloys during hot compression at 600 °C and different deformations

As the deformation increases to 60%, an apparent DRX occurs in all the alloys, causing the considerable grain refinement. The average grain sizes of S2, SC1 and SC2 alloys are 53.1, 42.5 and 29.7 μm, respectively, as shown in Fig. 4. From Figs. 3(c, f), it can be observed that the cracks in the S2 alloy are still apparent, whereas the intergranular cracks in the SC1 alloy are not apparent because of the grain refinement. Although the SC1 alloy has smaller grain size than the S2 alloy, the cracks in SC1 alloy are retained as the deformation increases. This alleviates the stress concentration at the GBs, which is responsible for the slight decrease in the peak stress of the SC1 alloy compared with the S2 alloy. In contrast, no cracks appear in the SC2 alloy, and the grains of SC2 alloy are finer and much more uniformly distributed. This contributes to the grain refinement strengthening and thus the corresponding highest peak stress, as shown in Fig. 2(b).

Figure 5 shows the misorientation distribution

of the S2, SC1 and SC2 alloys during the hot deformation, and the corresponding average misorientation angles are presented in Fig. 6. As the deformation increases, the volume fraction of LAGBs of the S2 alloy decreases from 80.2% to 55.9% and its average misorientation increases from 12.7° to 23.1°. This indicates that the dislocation slip dominates the deformation process. After trace amounts of Ce are added, the volume fractions of the LAGBs in the SC1 and SC2 alloys exhibit an increasing tendency, with the average misorientations of 8.7° and 9.1° at a deformation of 20%, and 12.4° and 7.3° at a deformation of 40%, respectively, which are smaller than those of the S2 alloy. This indicates that the dislocation slip remains the main deformation mechanism in SC1 and SC2 alloys when the reduction is less than 40%.

As the deformation increases from 20% to 40%, the volume fraction of LAGBs in the SC1 alloy decreases from 88.1% to 79.6%, while that of LAGBs in the SC2 alloy increases from 87.3% to 91.7%. This is due to the higher content of Ce in SC2 alloy (120×10^{-6}), which can completely consume the S impurities to form the Ce−S precipitates. Thus, the SC2 alloy contains a higher precipitate content than the SC1 alloy. During hot compression, both the particles and the dissolved Ce atoms can hinder the movement of dislocations, causing them to pile up and thereby increasing the volume fraction of the LAGBs.

When the deformation exceeds 40%, the DRX of the SC1 and SC2 alloys is significantly accelerated driven by the deformation storage energy, which results in a rapid increase in the content of HAGBs, as presented in Figs. 5(f, i). Moreover, the volume fractions of TBs in the SC1 and SC2 alloys also display an obvious increase. In Fig. 6, it can be seen that the average misorientations of the SC1 and SC2 alloys at a deformation of 60% are respectively 36.0° and 34.1°, an increase of approximately 50% compared with the S2 alloy. Such a variation indicates that the dominant role of twinning deformation during the hot deformation is obvious at the later stage of deformation due to the addition of trace Ce.

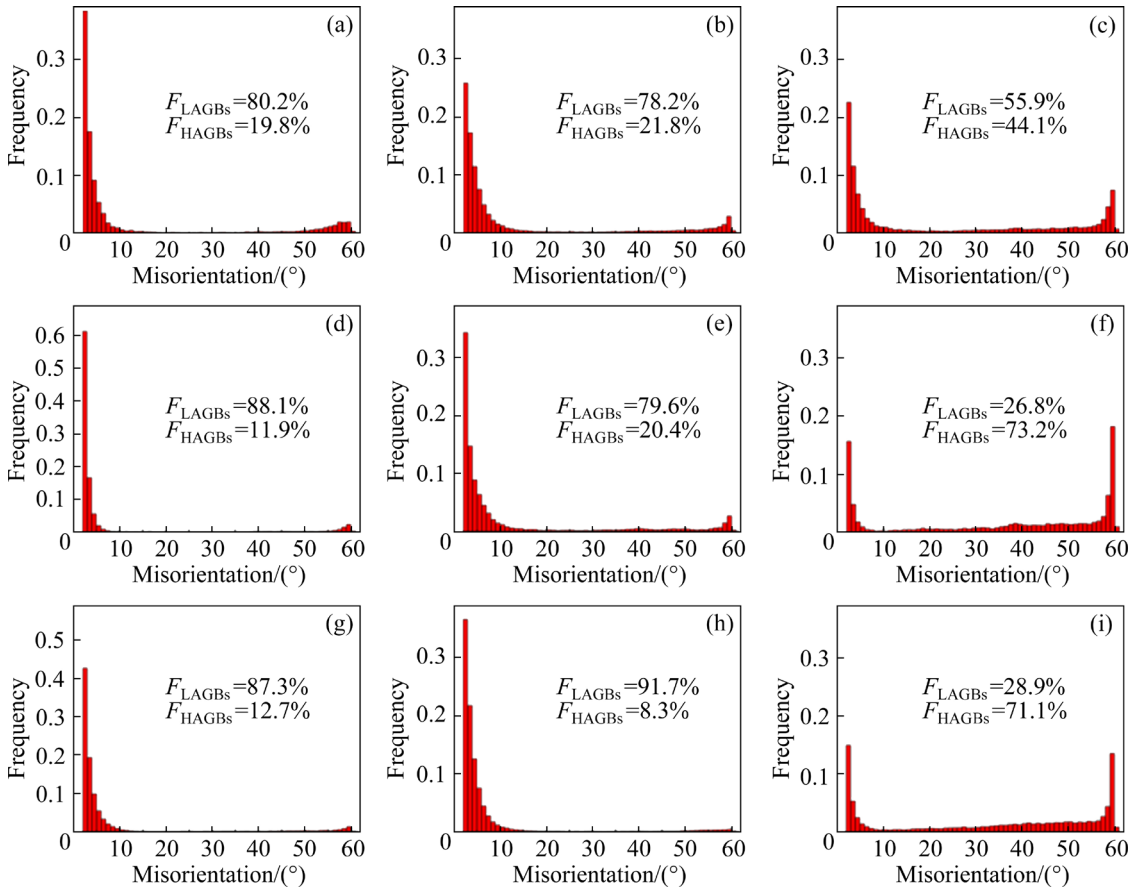

Fig. 5 Misorientation distributions of S2 (a–c), SC1 (d–f), and SC2 (g–i) alloys at different deformations during hot compression at 600 °C: (a, d, g) 20%; (b, e, h) 40%; (c, f, i) 60%

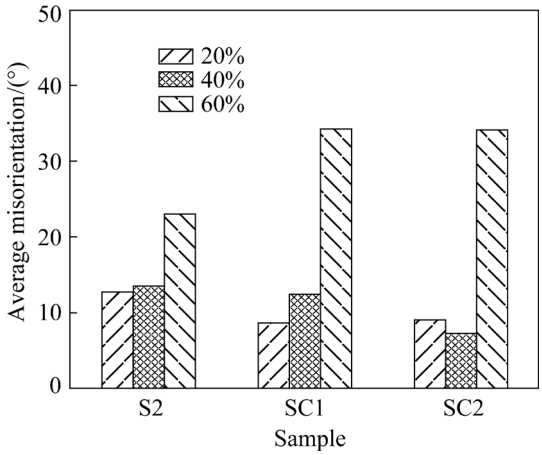

Fig. 6 Average misorientation of S2, SC1 and SC2 alloys at different deformations during hot compression at 600 °C

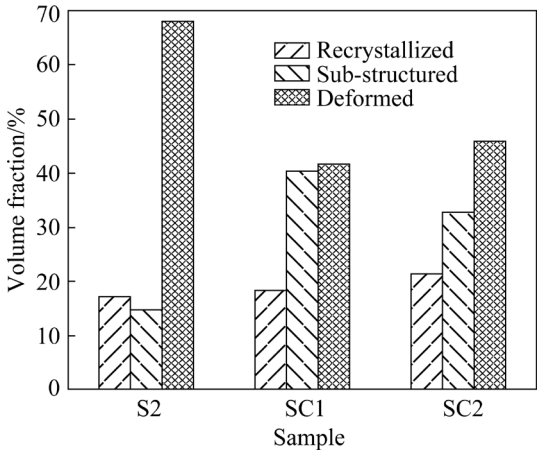

Fig. 7 Volume fractions of different types of grains in S2, SC1 and SC2 alloys at deformation of 60%

3.4 Dynamic recrystallization

Figure 7 presents the proportions of different types of grains in the S2, SC1 and SC2 alloys at the deformation of 60%. The volume fractions of the DRX, sub-structured and deformed grains in the S2 alloy are 17.2%, 14.8% and 68.0%, respectively. After trace amounts of Ce are added, the proportions of the DRX grains in the SC1 and SC2 alloys increase to 18.4% and 21.4%, respectively, whereas those of the deformed grains decrease to 40.1% and 32.9%, respectively. Therefore, it can be considered that even small amounts of Ce addition can promote the DRX of the S2 alloy.

Figure 8 shows the nucleation characteristics of the DRX grains in the S2 alloy. In Fig. 8(a), numerous DRX grains nucleate and grow at the interface between the original grains A and B.

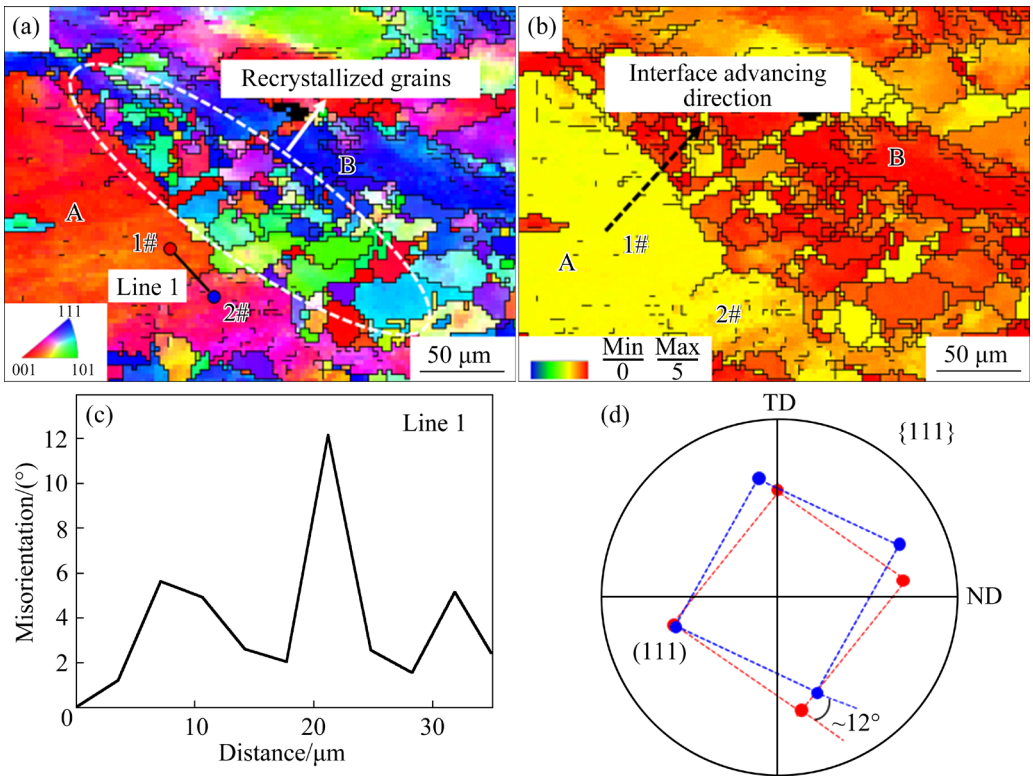

Fig. 8 Analysis of DDRX grain orientation of S2 alloy deformed at 600 °C: (a) Orientation map; (b) Corresponding Taylor factor graph; (c) Distribution of orientation difference of Line 1; (d) Crystallography orientation relationship between Grains 1# and 2#

Figure 8(b) provides the corresponding diagram of the Taylor factor, which is greater for Grain B than Grain A. Thus, the interface advances from A to B, thereby gradually decreasing the amount of ⟨111⟩-oriented grains. In addition, Grain A contains massive sub-grain boundaries, and there is a sudden change of ~12° between the sub-grains 1# and 2#, as presented in Fig. 8(c). The corresponding pole figure shown in Fig. 8(d) reveals that the orientation of the two sub-grains follows a ~12°/[111] specific crystallography relationship. Furthermore, the deformation storage energy of sub-grain 2# is greater than that of sub-grain 1# because of the relatively large Taylor factor (Fig. 8(b)). Therefore, sub-grain 2# likely undergoes DXR under this deformation condition, which is achieved by the continuous absorption of dislocations by the sub-grain boundaries near GBs. Such an orientation transformation is considered as a typical discontinuous dynamic recrystallization (DDRX) [25], mainly comprising three steps. First, the primary GBs migrate and bow out driven by the temperature and applied stress. Then, the continuous thermal deformation generates numerous dislocations at the arched area, forming strong strain gradients near the GBs. Finally, the sub-grain boundaries around the arched area increase the misorientation by absorbing dislocations or generating lattice rotation, thus forming an independent DRX grain.

Figure 9 provides the TEM images of the S2 alloy at the deformations of 20% and 40%, respectively. At the initial stage of compression, the GB slightly bows out, causing the dislocation density to increase significantly and thus the DXR grain begins to nucleate, as shown in Fig. 9(a). Then, with the increase of the deformation, sub-grains form and rotate, resulting in the formation of DXR grains, as presented in Fig. 9(b). Thus, the DDRX mechanism dominates the DRX of the S2 alloy.

After the addition of trace Ce, the recrystallization mechanism of the S2 alloy changes. Figure 10 shows the nucleation characteristics of the DRX grains in the SC1 alloy. The original grain is labeled as A, which has a ⟨110⟩ orientation, and the DRX grains are marked as 1#−5#. These DRX grains are formed inside the Grain A by in-situ transformation of the sub-grains. Such a process is a typical continuous dynamic recrystallization

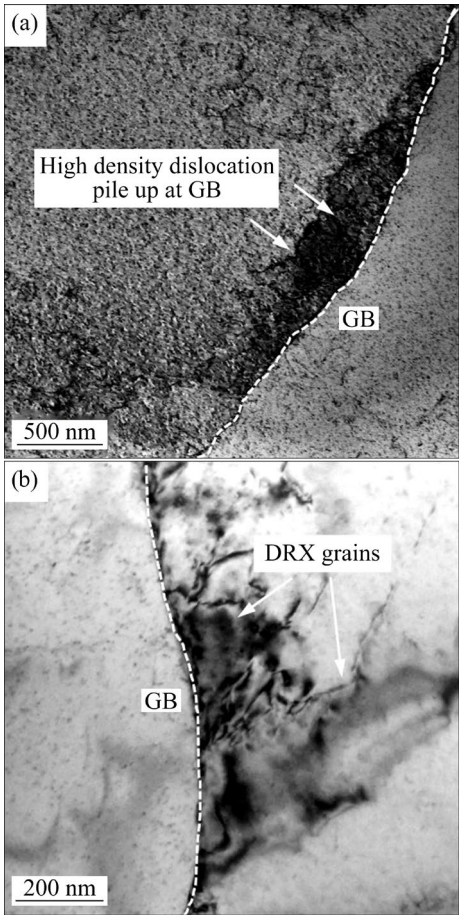

Fig. 9 TEM images of S2 alloy at deformations of 20% (a) and 40% (b)

(CDRX) mechanism [26]. Figure 10(c) presents the misorientation distribution of the Line 2, which reveals that the misorientations between adjacent DRX grains are greater than 20°. Nevertheless, the pole figure shown in Fig. 10(d) demonstrates that the DRX grains have a common rotation axis, close to [110]. Typically, the deformation storage energy of the primary grains with different orientations varies because of the different Taylor factors. The ⟨100⟩-oriented grains usually initiate few slip systems, therefore, they tend to undergo strong DRV to retain their orientations during the deformation. In contrast, the grains with ⟨110⟩ or ⟨111⟩ orientations are likely to stimulate DRX due to the excitation of more slip systems [27−29]. This is the fundamental reason for the appearance of DXR grains in the ⟨110⟩ or ⟨111⟩ grains in Cu−S−Ce alloy, as shown in Figs. 3(e, h).

In addition to the CDRX mechanism, the addition of Ce can also lead to twinning-induced DRX (TDRX) behavior in the S2 alloy, as shown in Fig. 11. The original grains are marked as A and B,

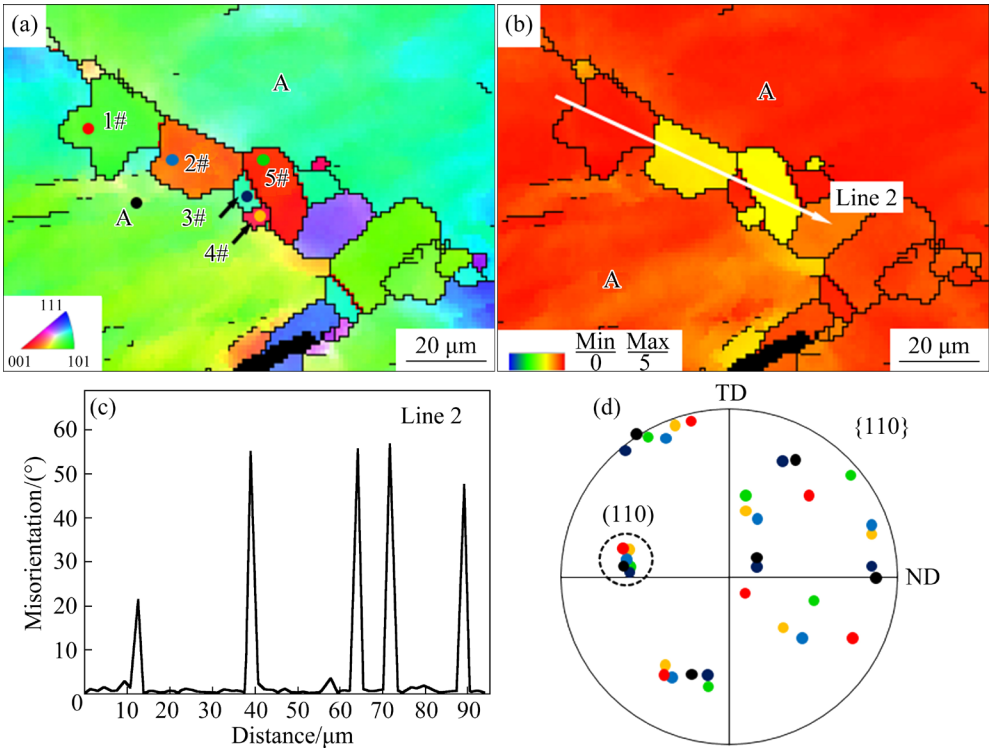

Fig. 10 Analysis of CDRX grain orientation in SC1 alloy deformed at 600 °C: (a) Orientation map; (b) Corresponding Taylor factor graph; (c) Distribution of orientation difference of Line 2; (d) {110} pole figure of parent and DRX grains

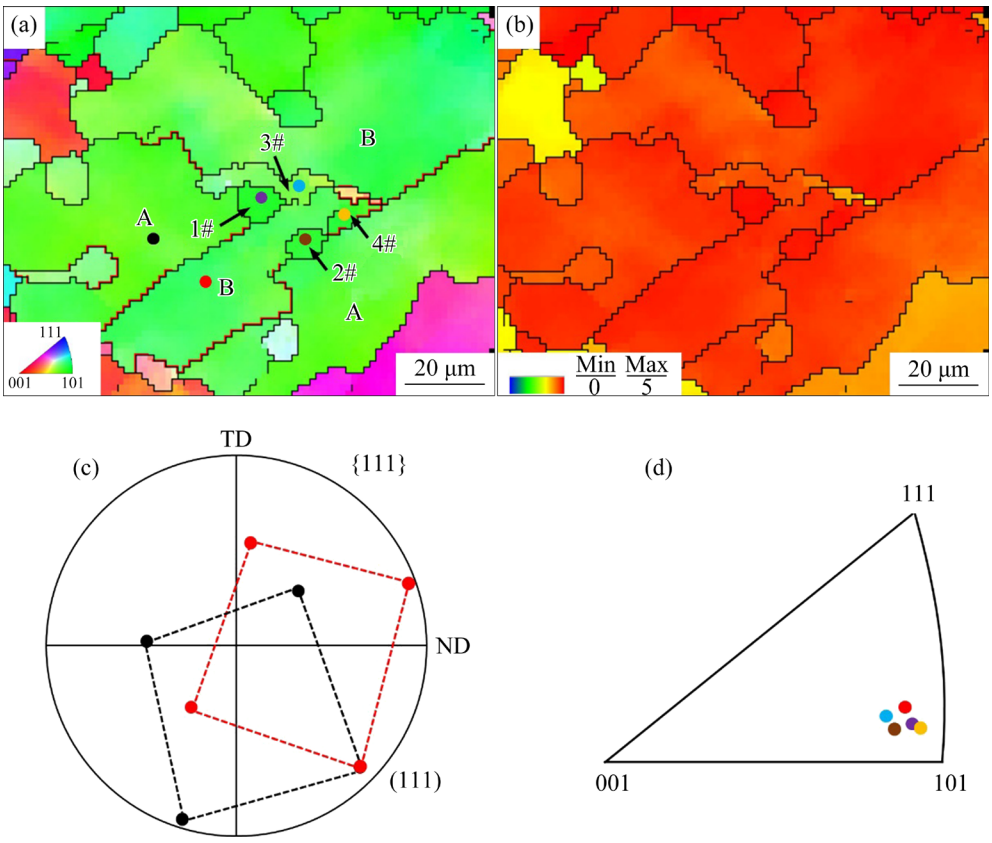

Fig. 11 Analysis of TDRX grain orientation in SC1 alloy deformed at 600 °C: (a) Orientation map; (b) Corresponding Taylor factor graph; (c) Crystallography orientation relationship between Grains A and B; (d) IPF of parent and DRX grains

the DRX grains are labeled as 1#−4#, and the Σ3 TBs are represented by red lines. Figure 11(c) presents the {111} pole figure of Grains A and B, which follows a crystallography orientation relation of [111]/60°. From Fig. 11(a), it is observed that these fine DRX grains nucleate at TBs, with the Taylor factors basically consistent with that of the parent grains, as illustrated in Fig. 11(b). Moreover, the IPF presented in Fig. 11(d) reveals that the orientations of DRX grains are also similar to those of the original grains. This recrystallization mechanism involves the transition from TBs to LAGBs, resulting from the interaction between different twins or the reaction between twins and dislocations that cause a mismatch on both sides of the GB [30].

Figure 12 shows the TEM images of the twins in the SC2 alloy at a deformation of 40%. It is clear that a large number of dislocations are generated inside the twins. During the deformation, the movement of these dislocations can accumulate strain on both sides of the TB. When the local strain reaches a certain critical value, the DRX grains begin to nucleate at the TB. Given that, it can be seen that the addition of Ce can transform the DRX mechanism of the Cu−S alloy from DDRX to CDRX and TDRX.

3.5 Texture evolution

Figure 13 shows the IPFs of the S2, SC1 and SC2 alloys during hot deformation. The major texture components and their volume fractions are presented in Fig. 14. Before compression, the ⟨111⟩ texture is dominant in the S2 and SC1 alloys, while the ⟨110⟩-oriented grains are the major texture component of the SC2 alloy (Fig. 1). During hot compression, the texture intensity of the S2 alloy gradually decreases from 5.23 to 2.04 with increasing the strain, as shown in Figs. 13(a–c). The proportion of ⟨111⟩-oriented grains decreases from 56.1% to 12.4%, whereas that of ⟨110⟩-oriented grains increases from 1.42% to 19.9%, as presented in Fig. 14(a). The content of ⟨100⟩ component remains unchanged. After trace amounts of Ce are added, the texture component and intensity of the S2 alloy significantly change.

At the initial deformation stage, both the major texture types of the SC1 and SC2 alloys have ⟨110⟩ orientation, with the volume fractions of 33.1% and 27% (Figs. 14(b, c)), and texture intensities of 2.01 and 2.06, respectively (Figs. 13(d, g)). With the increase of deformation amount, the volume fraction of ⟨110⟩ texture in the SC1 alloy first increases and then decreases obviously, while the proportion of ⟨100⟩-oriented grains gradually increases, with the texture intensity slightly increases compared to that of the S2 alloy. By comparison, the SC2 alloy undergoes a transition of ⟨110⟩ → ⟨111⟩ → random texture, with a considerable decrease in texture intensity compared with the S2 and SC1 alloys.

The textural evolution due to trace Ce addition is mainly related to the DRX and the precipitation behavior in the alloys. According to Figs. 8−12, the addition of Ce transforms the DRX of S2 alloy from DDRX to CDRX and TDRX mechanisms. It has been reported that both the occurrence of DDRX and CDRX are favor of the texture weakening [31−36]. Thus, the gradual decrease in texture intensity of the S2 alloy during hot deformation is attributed to the DDRX process.

Compared with the S2 alloy, the texture intensity of the SC1 alloy slightly increases when the deformation amount exceeds 20%, which results

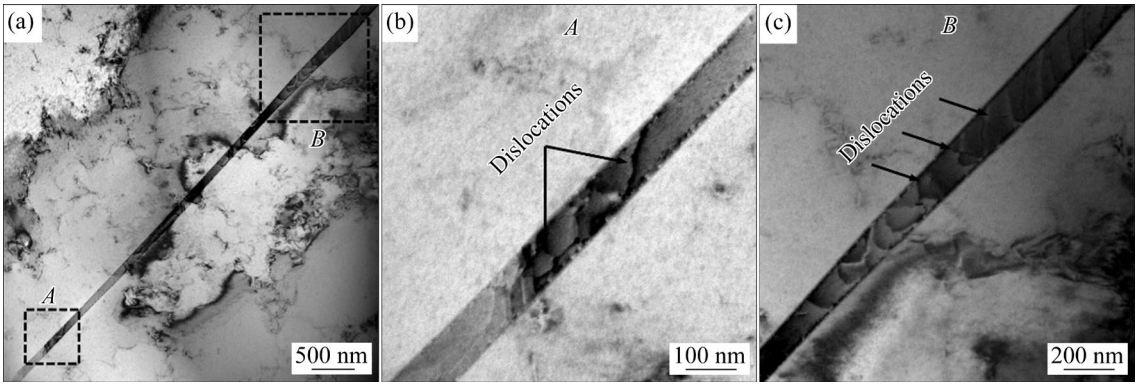

Fig. 12 TEM images of twins in SC2 alloy at deformation of 40%

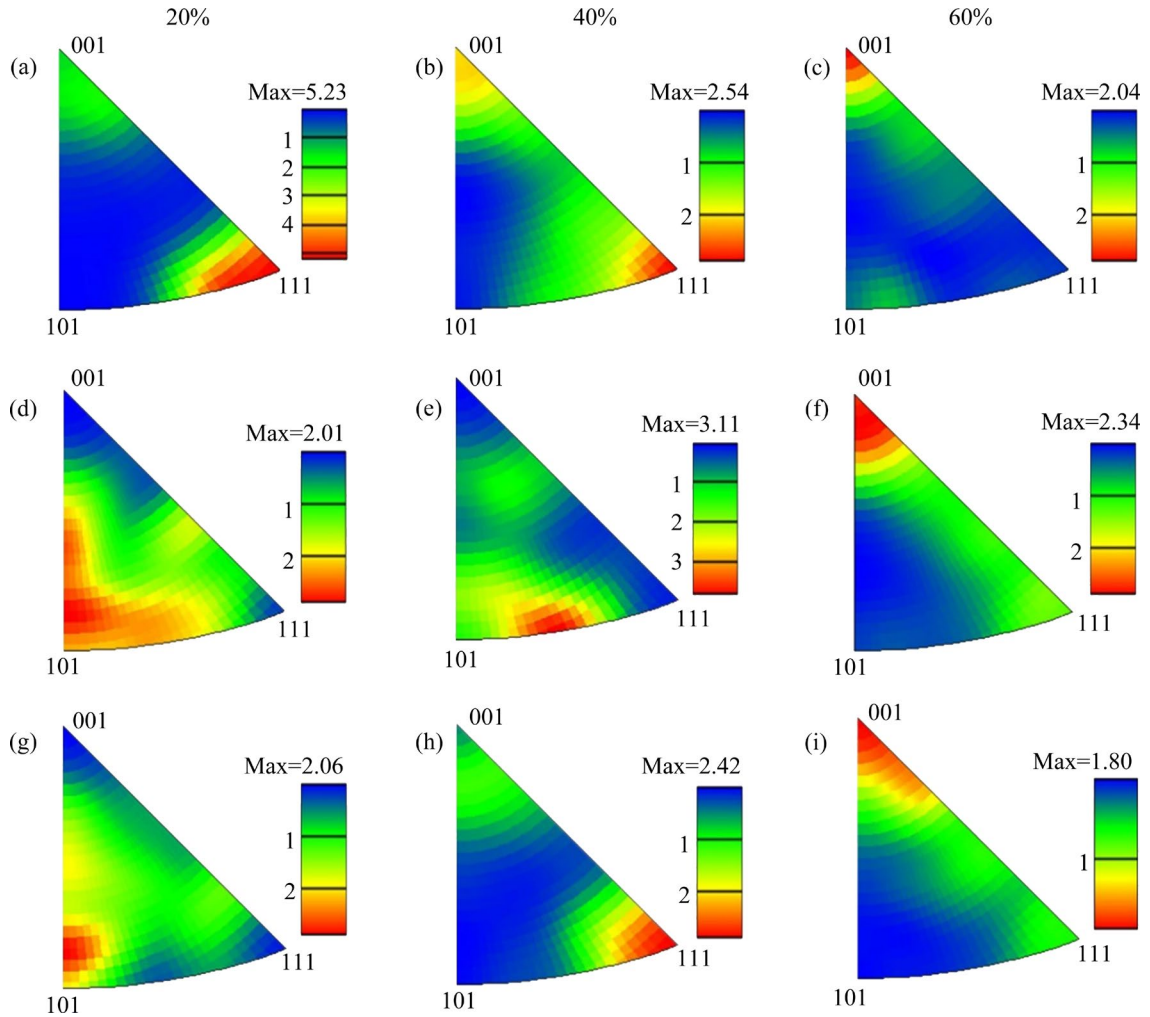

Fig. 13 IPFs of S2 (a–c), SC1 (d–f) and SC2 (g–i) alloys under different deformations during hot compression at 600 °C

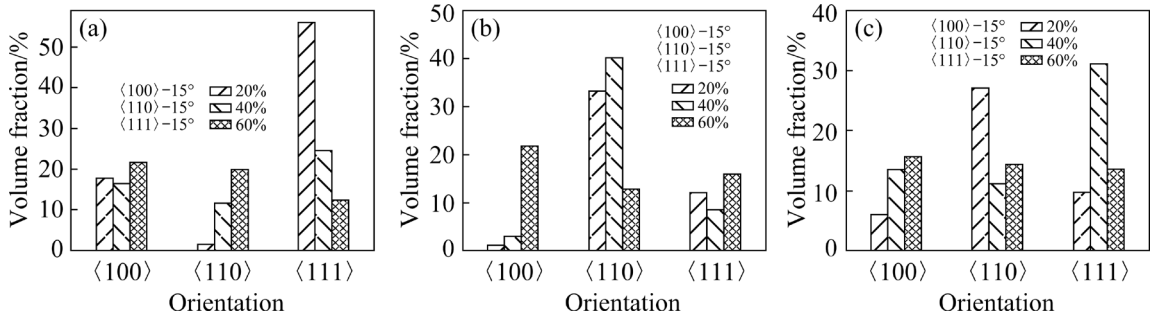

Fig. 14 Texture components and their volume fractions of S2 (a), SC1 (b) and SC2 (c) alloys under different deformations during hot compression at 600 °C

from the TDRX mechanism. From Fig. 11, it can be seen that the TDRX generally occurs in ⟨110⟩-oriented grains, the content of which in the SC1 alloy is much higher than that in the S2 alloy at the initial deformation stage, as shown in Figs. 14(a, b). Unlike the DDRX and CDRX grains, the orientation of the TDRX grains is similar to that of the parent grains. Therefore, such a process is detrimental to the texture weakening. In Fig. 7, the volume fractions of the DRX grains in the S2 and SC1 alloys are 17.2% and 18.4%, respectively. For the same recrystallization degree, DDRX in the S2 alloy is more conducive to grain orientation randomization, whereas TDRX in the SC1 alloy preserves the partial crystal orientation of the parent grains. This causes texture strengthening in the SC1

alloy at the later stage of deformation compared with the S2 alloy.

In contrast, the volume fraction of the DRX grains in the SC2 alloy (21.4%) is higher than that in the S2 alloy, as shown in Fig. 7. Moreover, the content of TBs in the SC2 alloy is lower than that in the SC1 alloy throughout the deformation process, which weakens the contribution of TDRX. In addition, the initial texture intensity of the SC2 alloy is much lower than that of the S2 alloy, thus the grain orientation is more randomized during the hot compression. Given that, it can be concluded that increasing the Ce content is more favorable for the texture weakening of the Cu−S alloy.

4 Conclusions

(1) During hot compression, the grain size of the S2 alloy gradually decreases with increasing Ce content, and its intergranular embrittlement is significantly inhibited after the addition of Ce.

(2) With the increase of strain, the dominant role of twinning-induced deformation tends to be obvious due to trace Ce addition.

(3) The addition of Ce can promote the DRX of the S2 alloy and transform its DRX mechanism from DDRX to CDRX and TDRX.

(4) The texture component and intensity of the S2 alloy considerably change after adding small amounts of Ce. Compared with the S2 and SC1 alloys, the grain orientation of the SC2 alloy is more randomized during the hot compression, which is ascribed to the promoted DRX.

CRediT authorship contribution statement

Ke-xing SONG: Conceptualization, Methodology, Project administration, Funding acquisition; **Yun-xiao HUA:** Writing − Original draft, Investigation, Data curation; **Hai-tao LIU:** Writing − Review & editing, Validation, Formal analysis; **Yan-min ZHANG:** Visualization, Supervision, Resources; **Chao-min ZHANG:** Methodology, Investigation; **Yan-jun ZHOU:** Visualization, Data curation; **Tao HUANG:** Supervision, Validation.

Declaration of competing interest

The authors declare that they have no known competing financial interests or personal relationships that could have appeared to influence the work reported in this paper.

Acknowledgments

This work was financially supported by the National Natural Science Foundation of China (Nos. 52071133, U21A2051), the Henan Province Science and Technology Tackling Key Problems Project, China (No. 222102230001), the Zhongyuan Scholar Workstation Funded Project, China (No. 224400510025), the Henan Key Research and Development Project, China (No. 221111230600), and Luoyang Major Science and Technology Innovation Special Project, China (No. 2201017A).

References

[1] WIMMER A, SMOLKA M, HEINZ W, DETZEL T, ROBL W, MOTZ C, EYERT V, WIMMER E, JAHNEL F, TREICHLER R, DEHM G. Temperature dependent transition of intragranular plastic to intergranular brittle failure in electrodeposited Cu micro-tensile samples [J]. Materials Science and Engineering: A, 2014, 618: 398−405.

[2] LAPORTE V, MORTENSEN A. Intermediate temperature embrittlement of copper alloys [J]. International Materials Reviews, 2009, 54: 94−116.

[3] SUN Z, LAITEM C, VINCENT A. Dynamic embrittlement at intermediate temperature in a Cu−Ni−Si alloy [J]. Materials Science and Engineering: A, 2008, 477: 145−152.

[4] HUA Yun-xiao, LIU Hai-tao, SONG Ke-xing, WANG Jiang-wei, ZHOU Yan-jun, HUANG Tao, LI Shao-lin, PENG Xiao-wen, ZHU Qian-qian. Trace sulfur-induced embrittlement of ultrahigh-purity copper [J]. Materials Science and Engineering: A, 2022, 848: 143397.

[5] LI Hai-hong, LIU Xiao, LI Yang, ZHANG Shi-hong, CHEN Yan, WANG Song-wei, LIU Jin-song, WU Jin-hu. Effects of rare earth Ce addition on microstructure and mechanical properties of impure copper containing Pb [J]. Transactions of Nonferrous Metals Society of China, 2020, 30: 1574−1581.

[6] LI Zan, LIU Ping, YANG Chao-yun, LI Xing, LUAN Yi-kun, LI Dian-zhong. Effect of rare earth elements on microstructure and mechanical properties of bainite/ martensite bearing steel [J]. Journal of Materials Research and Technology, 2023, 22: 1546−1557.

[7] WANG Chang-gang, MA Rong-yao, ZHOU Yang-tao, LIU Yang, DANIEL E F, LI Xiao-fang, WANG Pei, DONG Jun-hua, KE Wei. Effects of rare earth modifying inclusions on the pitting corrosion of 13Cr4Ni martensitic stainless steel [J]. Journal of Materials Science & Technology, 2021, 93: 232−243.

[8] ZHANG Tian, TAO You-rui, WANG Xue-yin. Constitutive behavior, microstructural evolution and processing map of extruded Al−1.1Mn−0.3Mg−0.25RE alloy during hot compression [J]. Transactions of Nonferrous Metals Society of China, 2014, 24: 1337−1345.

[9] DING Wan-wu, ZHAO Xiao-yan, CHEN Tai-li, ZHANG Hai-xia, LIU Xiao-xiong, CHENG Yan, LEI Dong-kai. Effect of rare earth Y and Al−Ti−B master alloy on the

microstructure and mechanical properties of 6063 aluminum alloy [J]. Journal of Alloys and Compounds, 2020, 830: 154685.

[10] LIAO Heng-cheng, XU He-ting, HU Yi-yun. Effect of RE addition on solidification process and high-temperature strength of Al−12%Si−4%Cu−1.6%Mn heat-resistant alloy [J]. Transactions of Nonferrous Metals Society of China, 2019, 29: 1117−1126.

[11] WANG Xue-zhao, WANG You-qiang, NI Chen-bing, FANG Yu-xin, YU Xiao, ZHANG Ping. Effect of Gd content on microstructure and dynamic mechanical properties of solution-treated Mg−*x*Gd−3Y−0.5Zr alloy [J]. Transactions of Nonferrous Metals Society of China, 2022, 32: 2177−2189.

[12] HANTZSCHE K, BOHLEN J, WENDT J, KAINER K U, YI S B, LETZIG D. Effect of rare earth additions on microstructure and texture development of magnesium alloy sheets [J]. Scripta Materialia, 2010, 63: 725−730.

[13] TONG Guo-dong, LIU Hai-feng, LIU Yao-hui. Effect of rare earth additions on microstructure and mechanical properties of AZ91 magnesium alloys [J]. Transactions of Nonferrous Metals Society of China, 2010, 20(s): 336−340.

[14] HUA Yun-Xiao, LIU Hai-tao, SONG Ke-xing, WANG Jiang-wei, GUO Yin-gang, TIAN Jing, GUO Hui-wen. Effect of cerium on microstructure, texture and properties of ultrahigh-purity copper [J]. Journal of Rare Earths, 2024, 42: 220−227.

[15] HUA Yun-xiao, LIU Hai-tao, SONG Ke-xing, PENG Xiao-wen, ZHANG Chao-min, ZHOU Yan-jun, HUANG Tao, GUO Xiu-hua, MI Xu-jun, WANG Qiang-song. Trace Ce addition for inhibiting Bi segregation induced embrittlement in ultrahigh-purity copper [J]. Materials Characterization, 2022, 194: 112352.

[16] CHEN Liang, ZHOU Bing-wen, HAN Jian-ning, XUE Yan-yan, JIA Fei, ZHANG Xing-guo. Effects of alloying and deformation on microstructures and properties of Cu−Mg−Te−Y alloys [J]. Transactions of Nonferrous Metals Society of China, 2013, 23: 3697−3703.

[17] HU Peng-hong, SONG Hong-wu, WANG Song-wei, CHEN Yan, ZHANG Shi-hong. Mechanisms of primary phase refinement and toughness improvement of Cu−2wt.%Ag−0.15wt.%La alloy through continuous extrusion forming [J]. Materials Science and Engineering: A, 2021, 819: 141521.

[18] PAN Zhen-ya, CHEN Jiang-biao, LI Jin-fu. Microstructure and properties of rare earth-containing Cu−Cr−Zr alloy [J]. Transactions of Nonferrous Metals Society of China, 2015, 25: 1206−1214.

[19] XU De-ye, ZHOU Meng, ZHANG Yi, TANG Shun-long, ZHANG Zhi-yang, LIU Yong, TIAN Bao-hong, LI Xu, JIA Yan-lin, VOLINSKY A A, LI De, LIU Qiu-jie. Microstructure and hot deformation behavior of the Cu−Sn−Ni−Zn−Ti(−Y) alloy [J]. Materials Characterization, 2023, 196: 112559.

[20] ZHANG Yi, VOLINSKY A A, TRAN H T, CHAI Zhe, LIU Ping, TIAN Bao-hong. Effects of Ce addition on high temperature deformation behavior of Cu−Cr−Zr alloys [J]. Journal of Materials Engineering and Performance, 2015, 24: 3783−3788.

[21] WANG Bing-jie, ZHANG Yi, TIAN Bao-hong, YAKUBOV V, AN Jun-chao, VOLINSKY A A, LIU Yong, SONG Ke-xing, LI Li-hua, FU Ming. Effects of Ce and Y addition on microstructure evolution and precipitation of Cu−Mg alloy hot deformation [J]. Journal of Alloys and Compounds, 2019, 781: 118−130.

[22] WANG Bing-jie, ZHANG Yi, TIAN Bao-hong, AN Jun-chao, VOLINSKY A A, SUN Hui-li, LIU Yong, SONG Ke-xing. Effects of Ce addition on the Cu−Mg−Fe alloy hot deformation behavior [J]. Vacuum, 2018, 155: 594−603.

[23] MIRZADEH H. Constitutive modeling and prediction of hot deformation flow stress under dynamic recrystallization conditions [J]. Mechanics of Materials, 2015, 85: 66−79.

[24] BAYLE B, BOCHER P, JONAS J J, MONTHEILLET F. Flow stress and recrystallisation during hot deformation of Cu−9%Sn alloys [J]. Materials Science and Technology, 1999, 15: 803−811.

[25] HEIDARZADEH A, SAEID T, KLEMM V, CHABOK A, PEI Y T. Effect of stacking fault energy on the restoration mechanisms and mechanical properties of friction stir welded copper alloys [J]. Materials & Design, 2019, 162: 185−197.

[26] KAIBYSHEV R, MALOPHEYEV S. Mechanisms of dynamic recrystallization in aluminum alloys [J]. Materials Science Forum, 2014, 794/795/796: 784−789.

[27] RAABE D, SCHLENKERT G, WEISSHAUPT H, LÜCKE K. Texture and microstructure of rolled and annealed tantalum [J]. Materials Science and Technology, 1994, 10: 299−305.

[28] RAABE D. Investigation of contribution of {123} slip planes to development of rolling textures in bee metals by use of Taylor models [J]. Materials Science and Technology, 1995, 11: 455−460.

[29] HÖLSCHER M, RAABE D, LÜCKE K. Rolling and recrystallization textures of BCC steels [J]. Steel Research International, 1991, 62: 567−575.

[30] MYSHLYAEV M M, MCQUEEN H J, MWEMBELA A, KONOPLEVA E. Twinning, dynamic recovery and recrystallization in hot worked Mg−Al−Zn alloy [J]. Materials Science and Engineering: A, 2002, 337: 121−133.

[31] ZHANG Dong-dong, LIU Chu-ming, JIANG Shu-nong, GAO Yong-hao, WAN Ying-chun, CHEN Zhi-yong. Effects of dynamic recrystallization mechanisms on texture evolution in Mg−Gd−Y−Zr−Ag alloy during hot compression [J]. Journal of Alloys and Compounds, 2023, 944: 169190.

[32] JIANG M G, XU C, YAN H, FAN G H, NAKATA T, LAO C S, CHEN R S, KAMADO S, HAN E H, LU B H. Unveiling the formation of basal texture variations based on twinning and dynamic recrystallization in AZ31 magnesium alloy during extrusion [J]. Acta Materialia, 2018, 157: 53−71.

[33] HUANG Ke, LOGÉ R E. A review of dynamic recrystallization phenomena in metallic materials [J]. Materials & Design, 2016, 111: 548−574.

[34] LI Jia-chen, WU Xiao-dong, CAO Ling-fei, LIAO Bin, WANG Yi-chang, LIU Qing. Hot deformation and dynamic recrystallization in Al−Mg−Si alloy [J]. Materials Characterization, 2021, 173: 110976.

[35] YANG Qiu-yue, MA Min, TAN Yuan-biao, XIANG Song,

ZHAO Fei, LIANG Yi-long. Microstructure and texture evolution of TB8 titanium alloys during hot compression [J]. Rare Metals, 2021, 40: 2917−2926.

[36] DU Hua-qiu, LI Feng, HUO Peng-da, WANG Yu. Microstructure evolution and ductility improvement mechanisms of magnesium alloy in interactive alternating forward extrusion [J]. Transactions of Nonferrous Metals Society of China, 2022, 32: 2557−2568.

微量稀土铈对含硫纯铜热变形行为的影响

宋克兴[1,2]，华云筱[1]，刘海涛[1,3]，张彦敏[1,3]，张朝民[1,3]，周延军[1,3]，皇 涛[1,3]

1. 河南科技大学 材料科学与工程学院，洛阳 471023；
2. 河南省科学院 材料研究所，郑州 450046；
3. 有色金属新材料与先进加工技术省部共建协同创新中心，洛阳 471023

摘 要：采用 Gleeble−1500 热模拟试验机在 600 ℃条件下进行热压缩变形，研究微量 Ce 添加对含微量硫纯铜组织和织构演化以及动态再结晶的影响。结果表明，随着 Ce 含量的增加，Cu−S(S2)合金的晶粒尺寸逐渐减小，由杂质元素 S 引起的晶界脆化得到显著抑制。Ce 的添加促进了 S2 合金的动态再结晶过程，其动态再结晶机制由不连续转变为连续和孪晶诱导共存机制。S2 合金的织构组分和强度随 Ce 含量的增加而发生改变，当 Ce 的添加量为 120×10^{-6} 时，合金晶粒取向更为随机化，这是由于动态再结晶的促进作用。

关键词：Ce 添加；杂质 S；超高纯铜；显微组织；动态再结晶；织构

(Edited by Xiang-qun LI)